


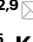

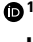



Topological bands and correlated states in helical trilayer graphene

Received: 29 March 2024

Accepted: 8 November 2024

Published online: 7 January 2025

 Check for updates

Li-Qiao Xia^{1,9} , Sergio C. de la Barrera^{1,2,9} , Aviram Uri^{1,9} ,
 Aaron Sharpe^{1,3} , Yves H. Kwan⁴, Ziyang Zhu⁵, Kenji Watanabe⁶,
 Takashi Taniguchi⁷ , David Goldhaber-Gordon^{1,5,8} , Liang Fu¹,
 Trithep Devakul^{1,8} & Pablo Jarillo-Herrero¹ 

The intrinsic anomalous Hall effect (AHE) is driven by non-zero Berry curvature and spontaneous time-reversal symmetry breaking. This effect can be realized in two-dimensional moiré systems hosting flat electronic bands but is not usually seen in inversion-symmetric materials. Here, we show that this physics is manifested in helical trilayer graphene—three graphene layers, each twisted in sequence by the same angle—although the system retains global in-plane inversion symmetry. We uncover a phase diagram of correlated and magnetic states at a magic twist angle of 1.8° , which is explained by a lattice relaxation that leads to the formation of large periodic domains where in-plane inversion symmetry is broken on the moiré scale. Each domain harbours flat topological bands with opposite Chern numbers in the two valleys. We find correlated states at multiple integer and fractional electron fillings per moiré unit cell and an AHE at a subset of them. The AHE disappears above a critical electric displacement field at one electron per unit cell, indicating a topological phase transition. We establish helical trilayer graphene as a platform that presents an opportunity to engineer topology due to its emergent moiré-scale symmetries.

The combination of strong electronic correlations and non-trivial band topology is fertile ground for exotic electronic phenomena. Driven by Berry curvature and orbital magnetization, the spontaneous emergence of the anomalous Hall effect (AHE) in non-magnetic materials is a notable example. It requires a periodic system that breaks both time-reversal symmetry (TRS) and the product of spatial inversion and TRS¹. Two-dimensional moiré materials are ideal for realizing these conditions because constituent layers with specific symmetries can be combined in a controlled way to engineer both the electronic band structure and its topology. Indeed, the AHE has been realized in various xy -inversion-broken moiré platforms, including graphene-based

systems^{2–18} and transition-metal dichalcogenides^{19–25}, where at least one of the van der Waals constituents intrinsically breaks xy -inversion (C_{2x}) symmetry. These systems rely on a single moiré to generate flat bands and strong correlations, whereas crystalline portions of the stack with broken C_{2x} symmetry (such as Bernal-stacked bilayer graphene) give rise to Berry curvature.

Three layers of graphene twisted with two independent angles, θ_{12} and θ_{23} , between the top two layers (1 and 2) and bottom two layers (2 and 3), respectively, unlock a new engineering degree of freedom by combining more than one moiré lattice, opening up a new way to generate Berry curvature. Although much of the two-angle space

¹Department of Physics, Massachusetts Institute of Technology, Cambridge, MA, USA. ²Department of Physics, University of Toronto, Toronto, Ontario, Canada. ³Materials Physics Department, Sandia National Laboratories, Livermore, CA, USA. ⁴Princeton Center for Theoretical Science, Princeton University, Princeton, NJ, USA. ⁵Stanford Institute for Materials and Energy Sciences, SLAC National Accelerator Laboratory, Menlo Park, CA, USA. ⁶Research Center for Electronic and Optical Materials, National Institute for Materials Science, Tsukuba, Japan. ⁷Research Center for Materials Nanoarchitectonics, National Institute for Materials Science, Tsukuba, Japan. ⁸Department of Physics, Stanford University, Stanford, CA, USA. ⁹These authors contributed equally: Li-Qiao Xia, Sergio C. de la Barrera, Aviram Uri. ✉e-mail: xialq@mit.edu; sdlb@mit.edu; aviramu@mit.edu; pjarillo@mit.edu

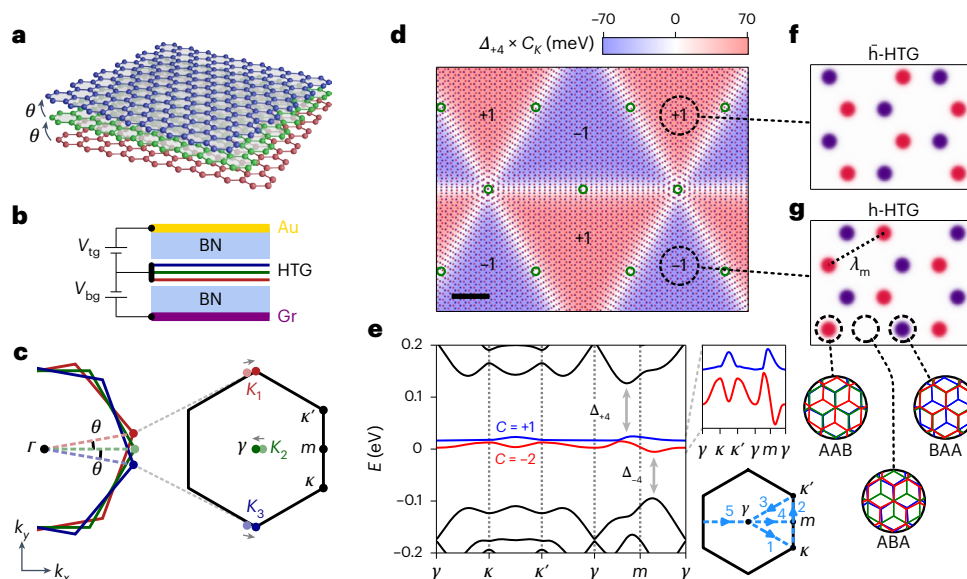


Fig. 1 | HTG. **a**, Schematic of the magic-angle HTG structure comprising three layers of graphene with successive layers rotated in the same direction by the same relative twist angle, $\theta \approx 1.8^\circ$. **b**, Circuit diagram of HTG surrounded by two hBN dielectric layers and top and bottom gate electrodes (Au and graphite, Gr, respectively) kept at electric potentials V_{tg} , V_{bg} relative to HTG. **c**, The rotated Brillouin zones of the three monolayers (left). Without lattice relaxation, the three Dirac points (light-coloured dots) lie on an arc. Including lattice relaxation (grey arrows), in the h-HTG and \bar{h} -HTG domains, they lie on a straight line, forming a periodic moiré Brillouin zone. **d**, Supermoiré structure of HTG including lattice relaxation. Crimson and purple dots represent AA stacking of the top and bottom pairs of adjacent layers, respectively. The small atomic lattice

relaxation is enough to form moiré-periodic domains (h-HTG and \bar{h} -HTG) hosting topological flat bands with large gaps, Δ_{44} , to remote bands. Scale bar, 50 nm. Background colour represents $\Delta_{44} \times C_K$ calculated for the local shift δ between the two moiré lattices, where C_K is the total Chern number per spin of the pair of flat bands in valley K . Green circles indicate centres of approximate C_{2z} rotation symmetry. **e**, Local non-interacting band structure in the h-HTG domain for valley K (Chern number of each flat band is indicated) with detail of flat bands and band path shown on the right. **f, g**, Moiré arrangement in the \bar{h} -HTG (**f**) and h-HTG (**g**) periodic domains, where C_{2z} symmetry is broken on the moiré scale. Circular callouts show the local atomic stacking of the three graphene layers in different regions.

$(\theta_{12}, \theta_{23})$ is filled with mutually incommensurate moiré lattices forming moiré quasicrystals²⁶, some angle combinations give rise to periodic domains on the moiré scale²⁷. Some commensurate combinations of twist angles, $p\theta_{12} = q\theta_{23}$ (p, q integers) (refs. 28–30), may locally escape quasiperiodicity once lattice relaxation is taken into account. Large supermoiré (or moiré of moiré) domains form, hosting periodic moiré lattices. Here, we demonstrate moiré engineering of local periodicity with $(p, q) = (1, 1)$ equi-angle helical trilayer graphene^{28,31,32}, which we henceforth refer to as simply HTG. In HTG, lattice-relaxation calculations predict the formation of large moiré-periodic domains, supporting electronic Bloch bands, emergent broken symmetries and Chern numbers defined within each domain^{33–35}. Although HTG is made purely of C_{2z} -symmetric components and is globally C_{2z} -symmetric, within each domain the system breaks C_{2z} symmetry (and also the product of C_{2z} and TRS, $C_{2z}T$), generating Berry curvature and non-trivial topology. Furthermore, the moiré bands can be sufficiently flat to spontaneously break TRS, leading to our observation of the AHE at certain fillings. Our observation of the AHE in HTG provides strong evidence for the emergent topological flat bands and brings to light the importance of local symmetries on length scales comparable to the interparticle distance, $n^{-1/2}$.

HTG

The three graphene layers in HTG, rotated sequentially by the same angle θ (Fig. 1a), form two moiré patterns between adjacent layer pairs. The two moiré lattices share the same lattice constant, $\lambda_m \approx a/\theta \approx 7.8$ nm for $\theta = 1.8^\circ$, but differ in orientation by θ (here, $a = 0.246$ nm is the atomic lattice constant of graphene). The misorientation between the two moiré patterns produces a position-dependent relative shift between them that is approximately periodic. The resulting supermoiré pattern has a lattice constant $\lambda_{sm} \approx \lambda_m/\theta \approx 250$ nm. In the absence of lattice relaxation, the two moiré patterns are mutually

incommensurate and the effective structure for low-energy electrons is a moiré quasicrystal²⁶. Lattice relaxation on the moiré scale is most prominent at small angles, $\theta \lesssim 1^\circ$, and is typically less important for larger angles³⁶. However, even at angles as large as $\theta = 1.8^\circ$, relaxation can have a profound effect on the supermoiré scale, favouring certain relative shifts between the two moiré patterns. The calculated relaxed structure of HTG forms large moiré-periodic domains, termed h-HTG and \bar{h} -HTG, that are related by a C_{2z} transformation^{33,35}. Figure 1d,f,g show the calculated relaxed moiré structure (Methods section ‘Relaxation’). Importantly, within each periodic domain, C_{2z} symmetry is spontaneously broken, allowing for Berry curvature and non-trivial topology.

The local non-interacting band structure within a domain is described by a pair of narrow-bandwidth topological bands (per spin and valley) separated by large gaps of order 100 meV from the remote bands (Fig. 1c,e). The absence of $C_{2z}T$ symmetry removes the protection of the three Dirac points (κ, κ', γ), thus gapping the charge-neutral point (Fig. 1e, inset) and endowing the flat bands with valley-contrasting Chern numbers $C_{K,K'} = \pm(1, -2)$ (Fig. 1e)^{33–35,37}. Electronic interactions, facilitated by the quenched kinetic energy of the flat bands, can spontaneously break the flavour degeneracy, similar to magic-angle graphene^{38–40}, resulting in spontaneous flavour ferromagnetism in spin (\uparrow, \downarrow), valley (K, K') and Chern-sublattice (A, B) space⁴¹. We will refer to the Chern-sublattice basis as sublattice for short hereinafter. Valley-polarized states break TRS and result in a non-zero net Chern number within each domain. In states where h-HTG and \bar{h} -HTG bands have different Chern numbers per valley, the network of domain walls between them hosts gapless edge modes^{33,35}.

Relaxation into periodic moiré domains comes at the cost of increased moiré aperiodicity within the domain walls³³. The overall structure of HTG is therefore a triangular tiling of moiré-periodic domains (on the scale of a few hundred nanometres) that are separated

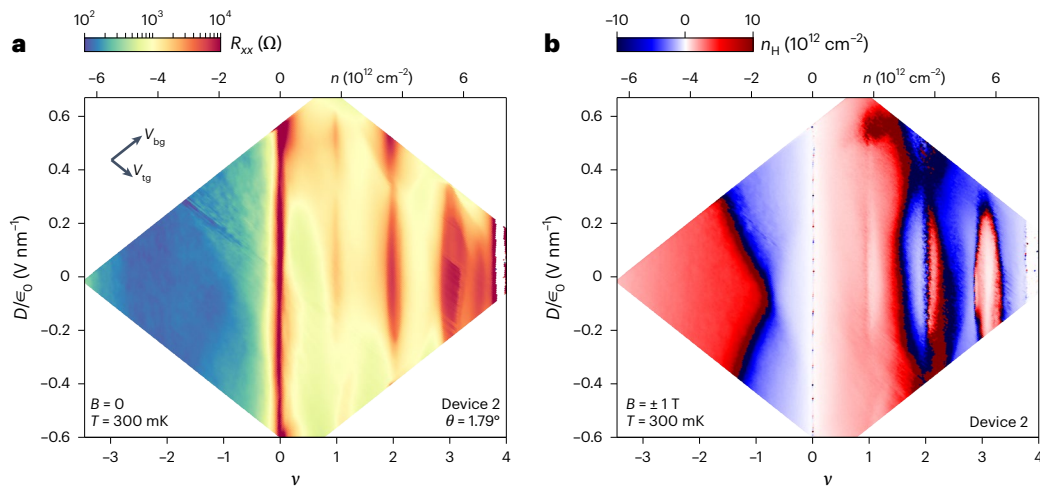


Fig. 2 | Strong electronic interactions. **a**, R_{xx} versus ν and D measured at $B = 0$ and $T = 300 \text{ mK}$, showing resistance peaks at charge neutrality ($\nu = 0$), at the moiré band gap ($\nu = 4$) and at the correlated states ($\nu = 1, 2, 3$ and $7/2$). **b**, Hall density n_H versus ν and D , acquired from antisymmetrizing R_{yx} at $B = \pm 1 \text{ T}$ and $T = 300 \text{ mK}$.

by gapless moiré-aperiodic domain walls (Fig. 1d). The global structure has approximate C_{2z} symmetry, as h-HTG and h-HTG are C_{2z} counterparts (Fig. 1f,g). We note that heterostrain can substantially deform the triangular supermoiré structure. However, the topology of the structure is expected to remain the same.

Correlated states

To probe the transport properties of HTG, we constructed dual-gated devices encapsulated by hexagonal boron nitride (hBN) (Methods section ‘Device fabrication’ and Extended Data Fig. 1). By applying voltages to the top and bottom gates (V_{tg} and V_{bg} , respectively; Fig. 1b), we controlled the electron density, n , and the perpendicular electric displacement field, D , independently while performing four-terminal magnetotransport measurements (Methods section ‘Electrical transport measurements’). The data shown throughout were measured using Device 2 unless stated otherwise.

Figure 2a shows the longitudinal resistance R_{xx} versus n and D measured at $B = 0$ and $T = 300 \text{ mK}$, where B is the applied out-of-plane magnetic field. The large resistance peak at $n = 7.45 \times 10^{12} \text{ cm}^{-2}$ indicates the gap between the flat and remote moiré bands at a filling of four electrons per moiré unit cell, $\nu = nA_{uc} = 4$, where A_{uc} is the area of the moiré unit cell. This reflects a twist angle of $\theta = 1.79^\circ$ (Methods section ‘Twist angle determination’ and Extended Data Fig. 2). Additional resistance peaks appear at integer fillings $\nu = 1, 2$ and 3 , indicative of flavour-symmetry-broken correlated electronic states. We observed similar behaviour in two more devices with twist angles 1.77° and 1.75° (Extended Data Figs. 3a and 4a) indicating that the magic angle for HTG is $\theta_m \approx 1.8^\circ$. For the appearance of correlated states in HTG devices with twist angles away from θ_m , see Supplementary Section 1 and Supplementary Table 2. Figure 2b shows the Hall density, n_H (Methods section ‘Calculation of the Hall density’), measured versus n and D (see also Supplementary Fig. 2 for a line cut). For electron doping, $n > 0$ and small D , n_H shows ‘resetting’ behaviour around $\nu = 1$, where n_H drops towards zero^{39,40}. Additionally, we find Van Hove singularities near $\nu = 1.5$ and 2.2 . Similarly to magic-angle twisted trilayer graphene, the Van Hove singularity at $\nu = 1.5$ may trigger a flavour-symmetry-breaking phase transition⁴². However, we cannot verify the change in flavour degeneracy due to the absence of clear quantum oscillations. At $\nu = 2$ under low $|D|$, field n_H shows a Dirac point or a gapped state behaviour as seen in magic-angle twisted trilayer graphene⁴². Near $\nu = 3$, Fig. 2b does not reflect the correct Hall density because we do not account for the strong AHE in this region (see details below) in our extraction of n_H . Therefore, the oval-shaped discontinuities at $\nu \approx 3$ and $\nu \approx 3.5$ do not reflect resets or Van Hove singularities.

The R_{xx} and n_H maps reveal pronounced electron–hole asymmetry. Correlated states only appear on the electron side, an observation we find consistently in all of our HTG devices (Extended Data Figs. 3 and 4, Supplementary Fig. 4 and Supplementary Table 2). The electron–hole asymmetry can be accounted for by introducing higher-order momentum-dependent tunnelling terms in the single-particle model (Methods section ‘Theoretical electronic band structure calculation’). Although these terms give only small corrections for alternating-twist trilayer graphene systems models, they prove crucial in modelling HTG. Extended Data Fig. 5 shows the non-interacting calculated Van Hove singularity, which is in agreement with our measurements for hole doping.

AHE

Figure 3a–f show the measured field-symmetrized R_{xx} and field-antisymmetrized R_{yx} as we sweep B up and down at different temperatures (see Methods section ‘Symmetrization and antisymmetrization’ for a description of the symmetrization and antisymmetrization procedure). We observe non-zero Hall resistance at $B = 0$ accompanied by pronounced magnetic hysteresis consistent with ferromagnetism near $\nu = 1$ and 3 . Considering the small intrinsic spin-orbit coupling in graphene, the ferromagnetism in our system is almost certainly of orbital origin rather than spin alone^{43,44}, as was shown in other graphene-based moiré systems in which AHE was previously reported^{8,45}. Combined with the topological flat bands (Fig. 1e)^{33–35}, this points to orbital ferromagnetism driven by Berry curvature in valley-polarized states⁴¹. Although R_{yx} is not quantized in our measurements, we would only expect to observe quantization from a single Chern domain. The magnitude of $|R_{yx}| \gtrsim 1.5 \text{ k}\Omega$ at $B = 0$ in our experiment reflects the net effect of multiple domains and the network of gapless domain walls between the R_{yx} contacts. We find multiple Barkhausen jumps and hysteresis in R_{yx} -versus- B loops that persist up to a temperature of $T_{hys} \approx 7.5 \text{ K}$. The R_{yx} discontinuity at $B = 0$ disappears at a Curie temperature of $T_C \approx 10.5 \text{ K}$ (see also Methods section ‘Extraction of Curie temperature’ and Extended Data Fig. 6), which is the highest reported among graphene-based moiré systems (Supplementary Table 1). The raw data, without symmetrization and antisymmetrization, shows strong mixing between R_{xx} and R_{yx} that we ascribe to strong anisotropy due to the gapless domain walls (Supplementary Figs. 8–10).

Notably, we find the AHE at $\nu = 1, 3$ in two additional devices with similar twist angles (Extended Data Figs. 3 and 4), demonstrating the robustness of the AHE in HTG. Apart from non-trivial band topology, another critical requirement for interaction-driven orbital magnetism is that the ground state favoured by strong correlations spontaneously

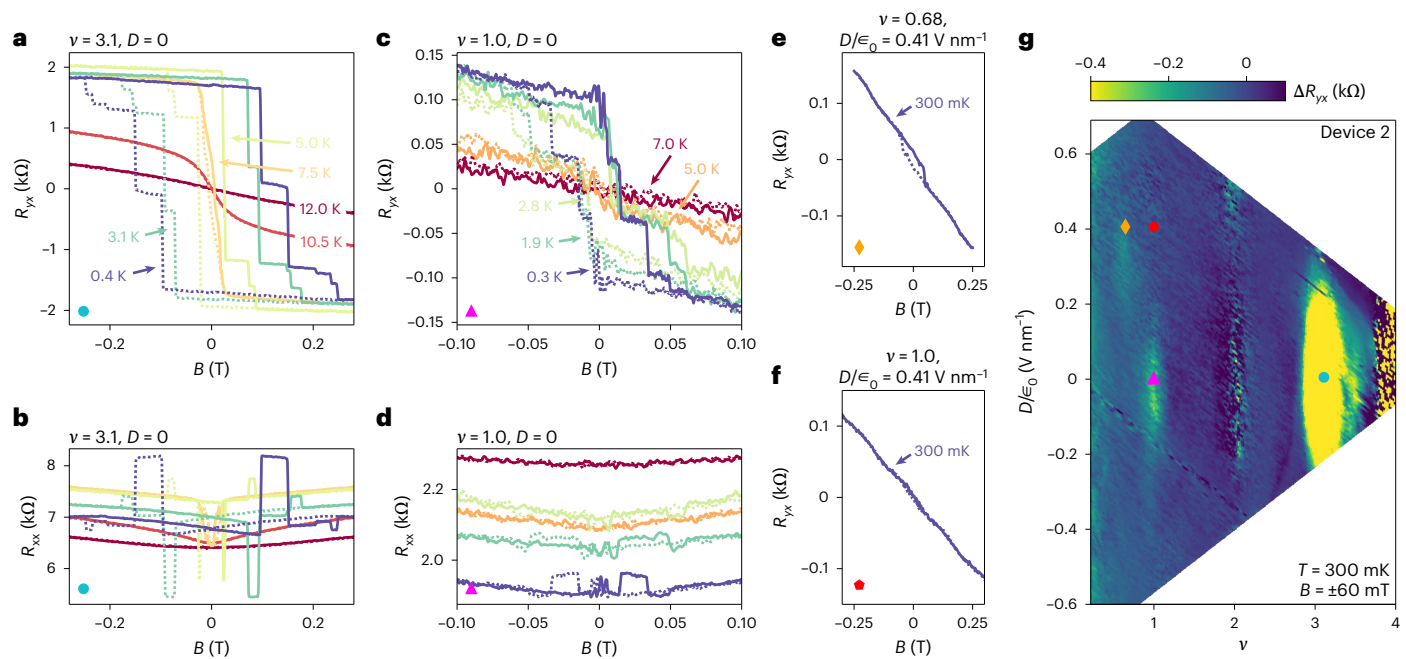


Fig. 3 | AHE. a, b, Field-antisymmetrized R_{yx} (**a**) and field-symmetrized R_{xx} (**b**) taken at $\nu = 3.1$ and $D = 0$ (cyan circle in **g**) while sweeping B up (solid) and down (dashed) at different temperatures as indicated. Temperature colour code in **b** is identical to **a**. **c, d**, Same as **a, b**, field-antisymmetrized R_{yx} (**c**) and field-symmetrized R_{xx} (**d**) taken at $\nu = 1$ and $D = 0$ (pink triangle in **g**). **e, f**, Same as **a**, taken

at $\nu = 0.68$, $D/\epsilon_0 = 0.41 \text{ V nm}^{-1}$ (orange diamond in **g**) and $T = 300 \text{ mK}$ showing AHE near $\nu = 2/3$. **f**, Same as **e**, taken at the same D and T but at $\nu = 1$ (red pentagon in **g**) showing no AHE. **g**, Field-trained ΔR_{yx} versus ν and D measured at $T = 300 \text{ mK}$ and $B = \pm 60 \text{ mT}$ after training at $B = \pm 1 \text{ T}$. Hot spots near $\nu = 1, 3$ and $\nu \approx 2/3$ indicate AHE.

breaks TRS, resulting in a net Chern number. In twisted monolayer-bilayer graphene, previous studies suggested that a close competition exists between different many-body ground states, including a valley-polarized state that breaks TRS and an intervalley-coherent state that preserves it^{5,9}. This potentially makes the AHE in twisted monolayer-bilayer graphene more sensitive to strain and twist angle disorder^{16,46}. In contrast, the robustness of the AHE in HTG suggests that valley-polarized states are strongly favoured at odd fillings. This aligns with the strong-coupling theory of HTG⁴¹.

Figure 3g provides an overview of the AHE in our system by plotting the difference ΔR_{yx} between R_{yx} taken at $B = \pm 60 \text{ mT}$ after training at high fields, $\pm 1 \text{ T}$, respectively. In the ranges $0.9 \lesssim \nu \lesssim 1.1$ and $2.8 \lesssim \nu \lesssim 3.3$, we find non-zero ΔR_{yx} indicating AHE, corroborated by the B -sweep hysteresis loops. In contrast, the correlated state near $\nu = 2$ shows no AHE, indicating a state that preserves TRS. At $\nu = 2$, theory points to a quantum valley-Hall state within the periodic domains⁴¹. The approximate symmetry of the AHE about $D = 0$ indicates that it does not rely on aligning the graphene trilayer to a substrate (see also Extended Data Fig. 1d).

There is a weaker ΔR_{yx} hot spot near $\nu = 2/3$ and $D/\epsilon_0 = 0.3 \text{ V nm}^{-1}$ (Fig. 3g). Figure 3e shows R_{yx} versus B measured at $\nu = 0.62$, $D = 0.41 \text{ V nm}^{-1}$ showing AHE. We note that at the same D field, there is no AHE at $\nu = 1$ (Fig. 3f); hence the AHE at fractional filling is a distinct state. This observation may indicate the presence of a topological charge density wave or fractional Chern insulator (Methods section ‘Hartree–Fock calculations at $\nu = 7/2, 2/3$ ’). The latter was predicted in HTG at $D = 0$ (ref. 33); however, whether the HTG bands favour fractional Chern insulators at large D fields is unclear. Thus, further investigation is required to identify the ground state. The appearance of the $\nu = 2/3$ feature only at one sign of D may be due to a slight difference in the effective screening from the top and bottom gates in combination with closely competing ground states that strongly depend on the interaction strength.

Lastly, there is an isolated resistive state centred on $\nu = 7/2$ and $D = 0$ (Fig. 2a), indicating a symmetry-broken phase. The temperature

dependence in Extended Data Fig. 7 shows that the $\nu = 7/2$ and $\nu = 3$ states occur on different temperature scales, indicating that they are distinct. Furthermore, we find AHE that extends from $\nu = 3$ to beyond $\nu = 7/2$ (Extended Data Fig. 8b), indicating the non-trivial topology of this state. At this filling, our Hartree–Fock calculations find closely competing topological states that include charge density waves⁴⁷ and a tetrahedral antiferromagnet (Methods section ‘Hartree–Fock calculations at $\nu = 7/2, 2/3$ ’ and Extended Data Fig. 9).

Indications of topological phase transitions

In Fig. 2a, the resistive peak at $\nu = 1$ centred at $D = 0$ disappears at $|D/\epsilon_0| \approx 0.35 \text{ V nm}^{-1}$ and reappears at higher $|D|$, suggestive of a phase transition involving a gap closure and re-opening. We do not find evidence for AHE at $|D/\epsilon_0| > 0.35 \text{ V nm}^{-1}$, and hence the high- $|D|$ phases preserve TRS. A leading theoretical possibility suggested by recent Hartree–Fock calculations of HTG⁴¹ is that at a critical displacement field, D_c , band inversion leads to a topological phase transition, with trivial bands emerging at $|D| > D_c$. Although a gapped intervalley-coherent state is also expected to show similar transport signatures, this possibility is unlikely^{33,41}. We observe similar behaviour of R_{xx} near $\nu = 2$, although at this filling, both the high- and low- $|D|$ phases do not exhibit AHE. Theory suggests⁴¹ that at $\nu = 2$, below D_c , the two valleys are equally occupied with bands of opposite Chern numbers, resulting in a zero net AHE. In contrast, above D_c , the bands are topologically trivial, which also results in no AHE.

Electrical switching of Chern domains

By sweeping ν in a fixed small magnetic field, $B \lesssim 0.2 \text{ T}$, we find that the sign of the AHE for a given ν depends on the sweep direction (Fig. 4a,b). This type of switching was observed in other moiré systems^{5,6,45} and was explained in terms of a sign flip in the orbital Zeeman energy per valley, $-\mathbf{M} \cdot \mathbf{B}$ (ref. 48). The sign flip is caused by a competition between the orbital magnetization induced by the self-rotation and centre-of-mass motion of the electronic wave packet¹. Here, \mathbf{M} is the total orbital magnetization, directed out of the plane. A calculation of

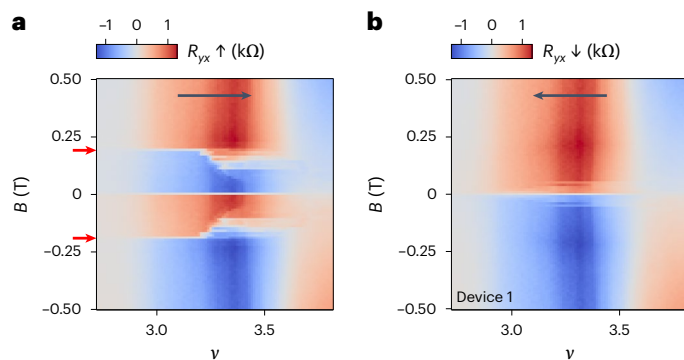


Fig. 4 | Density-induced switching near $\nu = 3$. **a**, Field-antisymmetrized R_{yx} versus ν and B while sweeping ν up as fast axis, measured on Device 1 at $D/\epsilon_0 = -0.15 \text{ V nm}^{-1}$. Red arrows indicate B_c . **b**, Same as **a**, only sweeping ν down.

the orbital magnetization $M(\nu)$ for an h-HTG domain, based on Hartree–Fock bands calculated at $\nu = 3$, is presented in Supplementary Section 2, demonstrating the sign change required for the above mechanism (Supplementary Fig. 5).

The hysteresis in $R_{yx}(\nu)$ shown in Fig. 4a,b exists over a large density range. Notably, it is present only at low magnetic fields and disappears abruptly as $|B|$ is increased above a critical value, $B_c \approx 0.2 \text{ T}$ (red arrows in Fig. 4a). Moreover, when sweeping ν up (Fig. 4a), R_{yx} in the high-positive-field regime ($B > B_c$) is almost identical to R_{yx} in the low-negative-field regime ($-B_c < B < 0$). This phenomenology is strikingly similar to what was previously observed in near-commensurate hBN-magic-angle twisted bilayer graphene, where local magnetic imaging revealed a spatial pattern of domains with different Chern numbers in the low-field regime⁴⁵. The similarity of the switching phenomena in HTG strongly suggests that Chern domains also play a role here. This is naturally explained by the different Chern numbers expected in h-HTG and h-HTG domains at integer ν (ref. 41). In Supplementary Section 3, we propose a detailed scenario explaining the observed unique hysteresis behaviour applied to HTG. However, we note that the multiple domains, gapless domain walls and many degrees of freedom may result in complex magnetotransport behaviour. Hence, our picture may be incomplete.

Scale-dependent symmetries

The dynamics of Bloch electrons in the presence of slowly varying external fields is described by the semiclassical model. The model considers wave packets of Bloch electrons—a distribution of width δk about some central momentum, k_0 . The wave packets are required to be localized both in real space and in momentum space. The real-space uncertainty, δx , should be small on the scale of the spatial variations of the external fields, whereas the narrow momenta distribution, δk , allows approximating the wave packet velocity as the group velocity at k_0 . The semiclassical model can be applied to HTG, where the moiré lattice provides the periodic potential and the supermoiré plays the role of the slowly varying external fields. Applying the semiclassical model to HTG is justified when the real-space size of the wave packet is much smaller than the supermoiré domains: that is, $\delta x \ll \lambda_{sm}$. Using the uncertainty relation $\delta x \delta k \geq 1/2$, we can relate the minimal size of the wave packet to the interparticle distance, $d = n^{-1/2}$, by $d \sim k_F^{-1} < \delta k^{-1} \lesssim \delta x$. At densities $n \geq 10^{11} \text{ cm}^{-2}$, the condition $d \ll \lambda_{sm}$ holds. This allows the use of a local band structure to describe the electronic properties in individual h-HTG and h-HTG domains. Even though at scales larger than λ_{sm} , HTG preserves C_{2z} symmetry, for scales corresponding to typical interparticle distances, $d \approx \lambda_m$, it breaks C_{2z} symmetry similar to other moiré systems that show AHE, such as twisted monolayer–bilayer graphene and hBN-aligned magic-angle twisted bilayer graphene. Thus, HTG demonstrates the importance of the

symmetries of a locally periodic system at the length scale of the interparticle distance.

Outlook

Our results demonstrate that engineering a supermoiré system to break C_{2z} symmetry on the moiré scale can induce topological bands despite the overall approximate C_{2z} symmetry of the system. The presence of gate-switchable Chern domains and a network of gapless edge modes, together with the high T_c and the high yield of samples exhibiting the AHE, establish HTG as an ideal platform for exploring orbital magnetism with Chern domain walls⁴⁹. Owing to its predicted homogeneous charge distribution, near-ideal quantum geometry³³ and small interaction-induced dispersion⁴¹, HTG is also promising for realizing exotic electronic phases, including zero-field fractional Chern insulating states^{33,47}. Lastly, superconductivity was recently predicted in HTG⁵⁰, opening the possibility of studying the interplay between topology and superconductivity in a graphene system.

Online content

Any methods, additional references, Nature Portfolio reporting summaries, source data, extended data, supplementary information, acknowledgements, peer review information; details of author contributions and competing interests; and statements of data and code availability are available at <https://doi.org/10.1038/s41567-024-02731-6>.

References

- Xiao, D., Chang, M.-C. & Niu, Q. Berry phase effects on electronic properties. *Rev. Mod. Phys.* **82**, 1959–2007 (2010).
- Sharpe, A. L. et al. Emergent ferromagnetism near three-quarters filling in twisted bilayer graphene. *Science* **365**, 605–608 (2019).
- Serlin, M. et al. Intrinsic quantized anomalous Hall effect in a moiré heterostructure. *Science* **367**, 900–903 (2020).
- Chen, G. et al. Tunable correlated Chern insulator and ferromagnetism in a moiré superlattice. *Nature* **579**, 56–61 (2020).
- Polshyn, H. et al. Electrical switching of magnetic order in an orbital Chern insulator. *Nature* **588**, 66–70 (2020).
- Chen, S. et al. Electrically tunable correlated and topological states in twisted monolayer–bilayer graphene. *Nat. Phys.* **17**, 374–380 (2021).
- Stepanov, P. et al. Competing zero-field Chern insulators in superconducting twisted bilayer graphene. *Phys. Rev. Lett.* **127**, 197701 (2021).
- Tschirhart, C. L. et al. Imaging orbital ferromagnetism in a moiré Chern insulator. *Science* **372**, 1323–1327 (2021).
- He, M. et al. Competing correlated states and abundant orbital magnetism in twisted monolayer–bilayer graphene. *Nat. Commun.* **12**, 4727 (2021).
- Polshyn, H. et al. Topological charge density waves at half-integer filling of a moiré superlattice. *Nat. Phys.* **18**, 42–47 (2022).
- Tseng, C.-C. et al. Anomalous Hall effect at half filling in twisted bilayer graphene. *Nat. Phys.* **18**, 1038–1042 (2022).
- Kuiri, M. et al. Spontaneous time-reversal symmetry breaking in twisted double bilayer graphene. *Nat. Commun.* **13**, 6468 (2022).
- Chen, G. et al. Tunable orbital ferromagnetism at noninteger filling of a moiré superlattice. *Nano Lett.* **22**, 238–245 (2022).
- Lin, J.-X. et al. Spin-orbit-driven ferromagnetism at half moiré filling in magic-angle twisted bilayer graphene. *Science* **375**, 437–441 (2022).
- Polski, R. et al. Hierarchy of symmetry breaking correlated phases in twisted bilayer graphene. Preprint at <https://arxiv.org/abs/2205.05225> (2022).
- Zhang, C. et al. Local spectroscopy of a gate-switchable moiré quantum anomalous Hall insulator. *Nat. Commun.* **14**, 3595 (2023).

17. Zhang, N. J. et al. Angle-resolved transport non-reciprocity and spontaneous symmetry breaking in twisted trilayer graphene. *Nat. Mater.* **23**, 356–362 (2024).
18. He, M. et al. Symmetry-broken Chern insulators in twisted double bilayer graphene. *Nano Lett.* **23**, 11066–11072 (2023).
19. Li, T. et al. Quantum anomalous Hall effect from intertwined moiré bands. *Nature* **600**, 641–646 (2021).
20. Anderson, E. et al. Programming correlated magnetic states with gate-controlled moiré geometry. *Science* **381**, 325–330 (2023).
21. Cai, J. et al. Signatures of fractional quantum anomalous Hall states in twisted MoTe₂. *Nature* **622**, 63–68 (2023).
22. Zeng, Y. et al. Thermodynamic evidence of fractional Chern insulator in moiré MoTe₂. *Nature* **622**, 69–73 (2023).
23. Foutty, B. A. et al. Mapping twist-tuned multiband topology in bilayer WSe₂. *Science* **384**, 343–347 (2024).
24. Park, H. et al. Observation of fractionally quantized anomalous Hall effect. *Nature* **622**, 74–79 (2023).
25. Xu, F. et al. Observation of integer and fractional quantum anomalous Hall effects in twisted bilayer MoTe₂. *Phys. Rev. X* **13**, 031037 (2023).
26. Uri, A. et al. Superconductivity and strong interactions in a tunable moiré quasicrystal. *Nature* **620**, 762–767 (2023).
27. Yang, C., May-Mann, J., Zhu, Z. & Devakul, T. Multi-moiré trilayer graphene: Lattice relaxation, electronic structure, and magic angles. *Phys. Rev. B* **110**, 115434 (2024).
28. Mora, C., Regnault, N. & Bernevig, B. A. Flatbands and perfect metal in trilayer moiré graphene. *Phys. Rev. Lett.* **123**, 026402 (2019).
29. Foo, D. C. W. et al. Extended magic phase in twisted graphene multilayers. *Phys. Rev. Res.* **6**, 013165 (2024).
30. Popov, F. K. & Tarnopolsky, G. Magic angle butterfly in twisted trilayer graphene. *Phys. Rev. Res.* **5**, 043079 (2023).
31. Mao, Y., Guerci, D. & Mora, C. Supermoiré low-energy effective theory of twisted trilayer graphene. *Phys. Rev. B* **107**, 125423 (2023).
32. Popov, F. K. & Tarnopolsky, G. Magic angles in equal-twist trilayer graphene. *Phys. Rev. B* **108**, L081124 (2023).
33. Devakul, T. et al. Magic-angle helical trilayer graphene. *Sci. Adv.* **9**, eadi6063 (2023).
34. Guerci, D., Mao, Y. & Mora, C. Chern mosaic and ideal flat bands in equal-twist trilayer graphene. *Phys. Rev. Res.* **6**, L022025 (2024).
35. Nakatsuji, N., Kawakami, T. & Koshino, M. Multiscale lattice relaxation in general twisted trilayer graphenes. *Phys. Rev. X* **13**, 041007 (2023).
36. Yoo, H. et al. Atomic and electronic reconstruction at the van der Waals interface in twisted bilayer graphene. *Nat. Mater.* **18**, 448–453 (2019).
37. Guerci, D., Mao, Y. & Mora, C. Nature of even and odd magic angles in helical twisted trilayer graphene. *Phys. Rev. B* **109**, 205411 (2024).
38. Cao, Y. et al. Unconventional superconductivity in magic-angle graphene superlattices. *Nature* **556**, 43–50 (2018).
39. Zondiner, U. et al. Cascade of phase transitions and dirac revivals in magic-angle graphene. *Nature* **582**, 203–208 (2020).
40. Wong, D. et al. Cascade of electronic transitions in magic-angle twisted bilayer graphene. *Nature* **582**, 198–202 (2020).
41. Kwan, Y. H., Ledwith, P. J., Lo, C. F. B. & Devakul, T. Strong-coupling topological states and phase transitions in helical trilayer graphene. *Phys. Rev. B* **109**, 125141 (2024).
42. Park, J. M., Cao, Y., Watanabe, K., Taniguchi, T. & Jarillo-Herrero, P. Tunable strongly coupled superconductivity in magic-angle twisted trilayer graphene. *Nature* **590**, 249–255 (2021).
43. Huang, C., Wei, N. & MacDonald, A. H. Current-driven magnetization reversal in orbital Chern insulators. *Phys. Rev. Lett.* **126**, 056801 (2021).
44. Sharpe, A. L. et al. Evidence of orbital ferromagnetism in twisted bilayer graphene aligned to hexagonal boron nitride. *Nano Lett.* **21**, 4299–4304 (2021).
45. Grover, S. et al. Chern mosaic and berry-curvature magnetism in magic-angle graphene. *Nat. Phys.* **18**, 885–892 (2022).
46. Lau, C. N., Bockrath, M. W., Mak, K. F. & Zhang, F. Reproducibility in the fabrication and physics of moiré materials. *Nature* **602**, 41–50 (2022).
47. Dong, J., Ledwith, P. J., Khalaf, E., Lee, J. Y. & Vishwanath, A. Many-body ground states from decomposition of ideal higher Chern bands: applications to chirally twisted graphene multilayers. *Phys. Rev. Res.* **5**, 023166 (2023).
48. Zhu, J., Su, J.-J. & MacDonald, A. H. Voltage-controlled magnetic reversal in orbital Chern insulators. *Phys. Rev. Lett.* **125**, 227702 (2020).
49. Zhang, C. et al. Manipulation of chiral interface states in a moiré quantum anomalous hall insulator. *Nat. Phys.* **20**, 951–956 (2024).
50. Long, M., Jimeno-Pozo, A., Sainz-Cruz, H., Pantaleón, P. A. & Guinea, F. Evolution of superconductivity in twisted graphene multilayers. *Proc. Natl Acad. Sci. USA* **121**, e2405259121 (2024).

Publisher's note Springer Nature remains neutral with regard to jurisdictional claims in published maps and institutional affiliations.

Springer Nature or its licensor (e.g. a society or other partner) holds exclusive rights to this article under a publishing agreement with the author(s) or other rightsholder(s); author self-archiving of the accepted manuscript version of this article is solely governed by the terms of such publishing agreement and applicable law.

© The Author(s), under exclusive licence to Springer Nature Limited 2025

Methods

Device fabrication

The van der Waals heterostructures were assembled in two parts using the standard dry-transfer technique. First, an hBN flake and a few-layer graphene strip were picked up by a poly(bisphenol A carbonate) stamp. This bottom stack was released onto a 285 nm SiO₂/Si substrate, followed by 12 h vacuum annealing at 350 °C to remove polymer residues. Then, tip cleaning was performed using the Contact Mode of a Bruker Icon XR atomic force microscope to clean the surface further. A monolayer graphene flake was cut into three pieces using a confocal laser-cut setup. A second poly(bisphenol A carbonate) stamp was used to pick up a hBN flake and the three graphene pieces subsequently. Before picking up the second and third pieces of graphene, the stage was rotated by 1.8° in the same direction to realize a helical stacking order. The pickup of graphene was done at room temperature to avoid the relaxation of the twist angle. The top stack was released onto the bottom stack at 150–170 °C.

The Hall bar was defined in a bubble-free region identified under an atomic force microscope. Patterns were defined using an Elionix ELS-HS50 electron-beam lithography system. A metallic top gate (25–65 nm Au with a 2–5 nm Cr or Ti adhesion layer) was deposited using a Sharon thermal evaporator. The device was connected using one-dimensional contacts (63–75 nm Au with a 2–5 nm Cr adhesion layer)⁵¹. Finally, the device was etched into a Hall bar geometry using reactive-ion etching.

Electrical transport measurements

Low-temperature electrical transport measurements were carried out in a helium-3 refrigerator with an 8 T perpendicular superconducting magnet and a base temperature of about 290 mK. A homemade twisted-pair copper tape filter with ~20 MHz cutoff frequency⁵² was thermally anchored at base temperature to guarantee the electron temperature of the device is the same as the phonon temperature. D.c. voltages were applied to the top and bottom gates using Keithley 2400/2450 source-measure units. The a.c. excitation of 1–10 nA at 16–24 Hz was applied using SR830 or SR860 lock-in amplifiers. The corresponding a.c. currents and voltages were measured using Stanford Research Systems SR830 or SR860 lock-in amplifiers, pre-amplified using DL-1211 current pre-amplifiers and DL-1201 voltage pre-amplifiers. The temperature was measured using a calibrated CX-1010-CU-HT-0.1L thermometer. $n = (\epsilon_{\text{BN}}\epsilon_0/e)(V_{\text{bg}}/d_{\text{bg}} + V_{\text{tg}}/d_{\text{tg}})$ and $D = (\epsilon_{\text{BN}}\epsilon_0/2)(V_{\text{bg}}/d_{\text{bg}} - V_{\text{tg}}/d_{\text{tg}})$ define n and D relations to V_{bg} and V_{tg} , where $\epsilon_{\text{BN}} = 3$ is the relative dielectric constant of hBN, ϵ_0 is the vacuum permittivity, e is the elementary charge and d_{bg} (d_{tg}) is the thickness of the bottom (top) hBN.

Dilution refrigerator measurements were performed in a Leiden Cryogenics CF-900 using a custom probe. The measurement lines are equipped with electronic filtering at the mixing chamber stage to obtain a low electron temperature in the device and reduce high-frequency noise. There are two stages of filtering: the wires are passed first through a cured mixture of epoxy and bronze powder to filter GHz frequencies and then low-pass RC filters mounted on sapphire plates filter MHz frequencies. Samples were mounted using a Kyocera custom 32-contact ceramic leadless chip carrier (drawing PB-44567-Mod with no nickel sticking layer under gold, to reduce magnetic effects). Stanford Research Systems SR830 lock-in amplifiers with NF Corporation LI-75A voltage pre-amplifiers were used to perform four-terminal resistance measurements. A 1 GΩ bias resistor was used to apply an a.c. bias current of up to 5 nA RMS at a frequency of 6.451 Hz. Keithley 2400 source-measure units were used to apply voltages to the gates.

In all measurements, the devices were cooled down under zero applied magnetic field.

Twist angle determination

Band structure calculations for the h-HTG and \bar{h} -HTG domains show large moiré band gaps at $\nu = \pm 4$, whereas the domain walls remain

gapless throughout the spectrum. At $\nu = \pm 4$, we expect the domain walls to form a metallic network, shunting the gapped periodic domains and somewhat lowering the resistance at these fillings, compared with a homogeneous insulating system. Nevertheless, we can still clearly identify resistive peaks at $\nu = 4$ and Landau levels emerging from the band extrema. We therefore use the features at $\nu = \pm 4$ to extract a twist angle for each device, with $n_{\nu=\pm 4} = \pm 8 \sin^2 \theta / \sqrt{3} a^2 \approx \pm 8 \theta^2 / \sqrt{3} a^2$, using $a = 0.246$ nm as the lattice constant for graphene.

We calibrate the twist angles for our HTG devices using the densities from which Landau levels emerge at integer fillings, particularly from $|\nu| = 4$ (Extended Data Fig. 2). We fit a series of integer slopes to the measured Landau level gaps (dips in R_{xx} emerging from $\nu = -4, 0, +4$) and resistive states at partial fillings (R_{xx} peaks at $\nu = 1, 2, 3$), using the density of $|\nu| = 4$, $n_{\nu=\pm 4}$, as a free parameter. The best fit across all fillings and sloped features yields for Device 2 $n_{\nu=\pm 4} = 7.45 \pm 0.17 \times 10^{12} \text{ cm}^{-2}$, corresponding to $\theta = 1.79 \pm 0.02^\circ$. Errors are estimated by aligning the collection of R_{xx} features to the left and right edges of each feature (R_{xx} minima for Landau level gaps or peaks of correlated states). See Supplementary Table 2 for the twist angles and error estimates of the other devices (errors estimated from R_{xx} peaks at integer filling for cases without clear Landau levels), along with a summary of the filling fractions ν for which correlated R_{xx} features and the AHE in R_{yx} are observed. The preponderance of correlated features and observations of the AHE clearly increases as the twist angle approaches 1.79° , although the precise behaviour for angles larger than $\sim 1.8^\circ$ remains to be explored in detail. This evolution of correlated features is especially evident in measurements of R_{xx} plotted versus ν for several devices in Supplementary Fig. 4.

We note that in the case of a slight mismatch between the two twist angles, $\theta_{12} \neq \theta_{23}$, the system relaxes to a structure similar to the equi-angle one, only with a smaller supermoiré unit cell (Methods section ‘Unequal twist angles and effects of twist angle disorder’ and Supplementary Fig. 7). Transport measurements only allow us to extract the resulting local twist angle θ in the periodic domains, which is between θ_{12} and θ_{23} .

Symmetrization and antisymmetrization

All the presented R_{xx} and R_{yx} data were symmetrized and antisymmetrized, respectively, with respect to the applied out-of-plane magnetic field B . Specifically, $R_{xx} = (R_{xx}^{\text{raw}}(B) + R_{xx}^{\text{raw}}(-B))/2$ and $R_{yx} = (R_{yx}^{\text{raw}}(B) - R_{yx}^{\text{raw}}(-B))/2$, where raw indicates raw data. This allows us to compensate for non-ideal Hall bar geometry and for anisotropies that we found to be important and ubiquitous in HTG. In measurements where B is the fast sweep axis, such as in Fig. 3a–f, the symmetrization and antisymmetrization were performed between curves of opposite sweep direction, so that $R_{yx} = (R_{yx}^{\text{raw}\uparrow}(B) - R_{yx}^{\text{raw}\downarrow}(-B))/2$ and $R_{xx} = (R_{xx}^{\text{raw}\uparrow}(B) + R_{xx}^{\text{raw}\downarrow}(-B))/2$ (here, the arrows indicate the sweep direction of B). In measurements where B was the slow axis, such as Fig. 4a,b, the antisymmetrization was performed between curves with opposite constant B : $R_{yx} = (R_{yx}^{\text{raw}}(B) - R_{yx}^{\text{raw}}(-B))/2$ and similarly for R_{xx} .

Calculation of the Hall density

We extract the Hall density $n_H = -e^{-1}(dR_{yx}/dB)^{-1}$ from R_{yx} measurements taken at ± 1 T according to $n_H = -(B_+ - B_-)/e(R_{yx}(B_+) - R_{yx}(B_-))$, where $B_{\pm} = \pm 1$ T, e is the elementary charge and $n_H > 0$ corresponds to electron doping. In a non-interacting system at low doping, $n_H \approx n$ and is expected to diverge near a Van Hove singularity. This is indeed the case for hole doping in our system. In contrast, on the electron doping, near $\nu = 1$, we find that n_H deviates below n , indicative of a flavour reset^{39,40}, similar to magic-angle twisted bilayer graphene and related moiré systems.

Extraction of Curie temperature

We extract T_C following ref. 53 by plotting R_{yx}^2 versus $|B/R_{xx}|$ at different temperatures. Such a plot for Device 2 is shown in Extended Data Fig. 6, taken at $\nu = 2.9$ and $D = 0$. We take R_{yx} as a proxy for the magnetization

M , reproducing an Arrott plot (M^2 versus M/H) (ref. 54). The intercept of a linear extrapolation of the high-field regime determines the magnetic state. At temperatures $T < 10.5$ K, we find a positive intercept indicating a ferromagnetic phase. At $T = 10.5$ K, the intercept is approximately zero, and above this temperature, the intercept is negative, indicating a transition to a paramagnetic phase; hence, the Curie temperature is approximately 10.5 K.

Theoretical electronic band structure calculation

The starting point for the single-particle band structure is the continuum model Hamiltonian³³. We first define the atomic lattice vectors for each layer as the columns of the matrix $A_\ell = \lambda_\ell R(\theta_\ell)A_0$, $R(\theta)$ is the counterclockwise rotation matrix, $(\theta_1, \theta_2, \theta_3) = (\theta, 0, -\theta)$ are the twist angles, $(\lambda_1, \lambda_2, \lambda_3) = (1, 1/\cos(\theta), 1)$ incorporates the biaxial strain in the relaxed domains, and $A_0 = a_0 \begin{pmatrix} 1 & \frac{1}{2} \\ 0 & \frac{\sqrt{3}}{2} \end{pmatrix}$, with $a_0 = 0.246$ nm. We use

italic text to indicate matrices and bold text to denote vectors. The monolayer reciprocal lattice vectors are then given by the columns of the matrix $G_\ell = 2\pi A_\ell^{-T}$. The generalization of the Bistritzer–MacDonald continuum model to the helical trilayer structure is

$$H(\mathbf{k}) = \begin{pmatrix} v_0 \boldsymbol{\sigma}_\theta \cdot [\mathbf{k} - k_\theta \hat{y}] + U & T_{12}(\mathbf{r} - \mathbf{d}_t) & 0 \\ T_{12}^\dagger(\mathbf{r} - \mathbf{d}_t) & v_0 \boldsymbol{\sigma} \cdot [\mathbf{k}] & T_{23}(\mathbf{r} - \mathbf{d}_b) \\ 0 & T_{23}^\dagger(\mathbf{r} - \mathbf{d}_b) & v_0 \boldsymbol{\sigma}_{-\theta} \cdot [\mathbf{k} + k_\theta \hat{y}] - U \end{pmatrix} \quad (1)$$

where $\boldsymbol{\sigma}_\theta = e^{-i\theta\sigma_z}(\sigma_x, \sigma_y)$ are Pauli matrices. This model describes the physics near the K points, $\mathbf{K}_\ell = G_\ell(2/3, 1/3)$ which lie on a vertical line, $(\mathbf{K}_1, \mathbf{K}_2, \mathbf{K}_3) = K_D \cos(\theta)\hat{x} + (k_\theta, 0, -k_\theta)\hat{y}$, where $K_D = \frac{4\pi}{3a_0}$ and $k_\theta = K_D \sin(\theta)$. The momentum \mathbf{k} is measured relative to the \mathbf{K}_2 point.

The interlayer tunnelling terms are given by

$$T_{\ell-1,\ell}(\mathbf{r}) = \sum_{n=0}^2 e^{-i\mathbf{Q}_{\ell-1,\ell}^n \cdot \mathbf{r}} \begin{pmatrix} w_{AA} & w_{AB} e^{-\frac{2\pi i n}{3}} \\ w_{AB} e^{\frac{2\pi i n}{3}} & w_{AA} \end{pmatrix} \quad (2)$$

where $\mathbf{Q}_{\ell-1,\ell}^n = (G_{\ell-1} - G_\ell)\mathbf{m}_n$, with $\mathbf{m}_0 = (0, 0)$, $\mathbf{m}_1 = (-1, 0)$ and $\mathbf{m}_2 = (-1, -1)$. Explicitly, $\mathbf{Q}_{12}^n = \mathbf{Q}_{23}^n = \mathbf{q}_0 - \mathbf{q}_n$, where $q_{n,x} + iq_{n,y} = -ik_\theta e^{\frac{2\pi i n}{3}}$. The h-HTG and \bar{h} -HTG regions are modelled by choosing the displacements $\mathbf{d}_t - \mathbf{d}_b = \pm \boldsymbol{\delta}$, respectively, where $\boldsymbol{\delta} = \frac{1}{3}(\mathbf{a}_2 - \mathbf{a}_1)$ and $\mathbf{a}_{1,2} = \frac{4\pi}{3k_\theta}(\pm \frac{\sqrt{3}}{2}, \frac{1}{2})$ are the moiré lattice vectors. The layer potential U models the effect of the displacement field. We use parameters $v_0 = 8.8 \times 10^5$ m s⁻¹, $w_{AB} = 110$ meV and $w_{AA} = 75$ meV.

To capture the particle-hole asymmetry, it is crucial to include the effect of longer-range interlayer tunnelling terms: that is, momentum-dependent tunnelling. This arises due to the non-local components of the interlayer tunnelling term, which we take to be^{55,56}

$$t(\mathbf{r}) = -te^{-(R-a_{cc})/r_0} \frac{r^2}{R^2} + t_\perp e^{(R-d)/r_0} \frac{d^2}{R^2} \quad (3)$$

where $r = |\mathbf{r}|$, $R = \sqrt{r^2 + d^2}$, $d = 3.35$ Å, $r_0 = 0.453$ Å, $t = 2.7$ eV, $t_\perp = 0.48$ eV. We define the Fourier transform of the tunnelling as $\tilde{t}(\mathbf{k}) = |A_0|^{-1} \int e^{-i\mathbf{k} \cdot \mathbf{r}} t(\mathbf{r}) d\mathbf{r}$. Because the momenta \mathbf{k} of relevance to the low-energy physics are close to the \mathbf{K} point, the value of the tunnelling evaluated at $\tilde{t}(\mathbf{K})$ is most important and determines the effective tunnelling parameter w in the Bistritzer–MacDonald model. The first-order correction due to the non-local tunnelling can be taken into account by expanding $t(\mathbf{k}) \approx t_0[1 + \xi(|\mathbf{k}| - K_D) + O((|\mathbf{k}| - K_D)^2)]$, where $t_0 \approx 0.11$ eV and $\xi \approx -2.1$ Å. Moiré scale lattice relaxation is expected to reduce the tunnelling between AB sublattices, which we take into account by uniformly scaling the AB tunnelling strength by an overall factor

w_{AB}/w_{AA} . Operationally, implementing the above amounts to replacing $T_{\ell-1,\ell}(\mathbf{r})$ with $T_{\ell-1,\ell}(\mathbf{k}, \mathbf{r})$, where

$$T_{\ell-1,\ell}(\mathbf{k}, \mathbf{r}) = \sum_{n=0}^2 e^{i\mathbf{Q}_{\ell-1,\ell}^n \cdot \mathbf{r}} (1 + \xi(|\mathbf{K}_2 + \mathbf{k} + G_\ell \mathbf{m}_n| - K_D)) \begin{pmatrix} w_{AA} & w_{AB} e^{-\frac{2\pi i n}{3}} \\ w_{AB} e^{\frac{2\pi i n}{3}} & w_{AA} \end{pmatrix} \quad (4)$$

is a tunnelling term whose strength depends on the momentum \mathbf{k} . Note that the factor containing \mathbf{k} appears on the right of those containing \mathbf{r} (which is important, as the two do not commute).

Hartree–Fock calculations at $\nu = 7/2, 2/3$

In this section, we perform self-consistent Hartree–Fock calculations in moiré-periodic h-HTG at non-integer fillings $\nu = 7/2, 2/3$, the same fillings where correlated features were observed in Fig. 3. To the non-interacting Hamiltonian in Section 7, we apply layer potentials $U, 0, -U$ on the three layers to mimic the effect of an external displacement field. For simplicity, the momentum-dependent tunnelling is not included in this analysis. Owing to the large energy gap to the remote bands, we project our calculations into the two central bands per flavour (spin and valley). We add dual-gate screened density-density interactions $V(q) = \frac{e^2}{2\epsilon_0 \epsilon_r q} \tanh qd_{sc}$, where the gate screening length is $d_{sc} = 25$ nm, and the effect of the hBN dielectric and remote bands is phenomenologically captured with the relative permittivity $\epsilon_r = 8$. The interaction term is normal-ordered with respect to the average density of the central bands at charge neutrality. To allow for gapped states at non-integer fillings within mean-field theory, we allow translation symmetry-breaking (TSB) by enlarging the unit cell. We allow breaking of all flavour and discrete rotational symmetries. Further details of the Hartree–Fock procedure are provided in ref. 41.

At $\nu = 7/2$ (Extended Data Fig. 9a–f), we additionally let the system break translation symmetry by doubling the unit cell length along both moiré axes (quadrupling the area of the unit cell). We find that the lowest-energy solution is a gapped state with TSB, as shown by the negative value of ΔE , which is defined as the Hartree–Fock energy per moiré unit cell measured relative to the best translation-symmetric solution. Its density matrix is consistent with fully filling all bands except a $|C| = 2$ band (corresponding to a B sublattice band in h-HTG), which is half-filled and reconstructed by TSB and spatially dependent spin rotations. Although the charge density is moiré-periodic (Extended Data Fig. 9a), the quadrupling of the unit cell is revealed by the non-coplanar spin texture (Extended Data Fig. 9b), which forms a tetrahedral antiferromagnet similar to that theoretically proposed in twisted monolayer–bilayer graphene and twisted double-bilayer graphene in ref. 57. If we restrict the calculation to maintain spin collinearity, we find two other spin-polarized solutions that realize a C_{3v} -symmetric charge density wave and a stripe charge density wave, respectively (Extended Data Fig. 9c,d). The stripe charge density wave is reminiscent of that proposed in ref. 10 to explain transport experiments in twisted monolayer–bilayer graphene. All three solutions are $|C| = 1$ states that preserve valley $U(1)_v$ symmetry and closely resemble the candidate ‘strong-coupling’ TSB orders expected from half-filling an ideal $|C| = 2$ band^{47,57}. The close energetic competition between the different orders (Extended Data Fig. 9e) points towards the ideality of the topological bands in h-HTG. $|\Delta E|$ decreases monotonically as a function of U , suggesting that the TSB state is weakened in a displacement field, although the U -dependence of the charge gap is less consistent (Extended Data Fig. 9f). Although the TSB solutions remain energetically favoured for the large range of interlayer potentials studied, we caution that Hartree–Fock tends to overestimate gaps and symmetry-breaking, such that beyond mean-field theory, the threshold value of U where the system recovers symmetry is expected to be reduced.

In Extended Data Fig. 9g,h, we show analogous results for $\nu = 2/3$, where we allow TSB to enlarge the unit cell threefold along both moiré axes. We again find the presence of gapped TSB solutions, although the gap size and TSB energy gain $|\Delta E|$ are smaller and non-monotonic in U . Interestingly, we find a window of non-zero interlayer potentials, slightly above/at the theoretical topological transition for $\nu = 1$ (ref. 41), where $|\Delta E|$ is locally maximal and the Hartree–Fock gap remains large. This suggests the possibility of a correlated state that only emerges at a non-zero displacement field. However, the presence of several closely competing states, multiple partially filled flavours and sensitive dependence on system parameters prevent an unambiguous interpretation of the Hartree–Fock results. We leave a more detailed theoretical investigation of the correlated physics at $\nu = 2/3$ to future work.

Relaxation

When considering the atomic arrangement of twisted graphene systems within a single moiré unit cell, it has been shown that for $\theta \geq 1^\circ$, lattice relaxation does not have a substantial effect on the moiré scale³⁶. This effect remains very small at 1.8° and does not depend on twist angle variations. However, even at large angles, as high as 1.8° , lattice relaxation can profoundly affect the relative shift between moiré-12 and moiré-23—the two moiré patterns in HTG. This shift allows the formation of the periodic h-HTG and \bar{h} -HTG domains.

To calculate the relaxation of the HTG system, we employ a continuum relaxation model in local configuration space⁵⁸. Therefore, instead of formulating the problem in real space, we adopt configuration space, which describes the local environment of every position in layer L_i and bypasses a periodic approximation⁵⁹. Every position in real space \mathbf{r} in L_i can be uniquely parametrized by three shift vectors $\mathbf{b}^{i \rightarrow j}$ for $j = 1, 2, 3$ that describes the relative position between any point in real space \mathbf{r} with respect to all three layers. Note that $\mathbf{b}^{i \rightarrow j} = \mathbf{0}$ if $i = j$ because the separation between a position with itself is 0, which leads to a four-dimensional configuration space.

For a given real space position \mathbf{r} , the following linear transformation uniquely maps between the real space position \mathbf{r} and the local configuration space component in layer i with respect to layer j $\mathbf{b}^{i \rightarrow j}$:

$$\mathbf{b}^{i \rightarrow j}(\mathbf{r}) = (E_j^{-1} E_i - \mathbf{1}) \mathbf{r}, \quad (5)$$

where E_i and E_j are the unit cell vectors of layers i and j respectively, rotated by θ_{ij} . In the trilayer system, there is no simple linear transformation between real and configuration space. The relation between the displacement field defined in real space, $\mathbf{U}^{(i)}(\mathbf{r})$, and in configuration space, $\mathbf{u}^{(i)}(\mathbf{b})$, can be found by evaluating $\mathbf{u}^{(j)}(\mathbf{b})$ at the corresponding $\mathbf{b}^{i \rightarrow j}(\mathbf{r})$ and $\mathbf{b}^{i \rightarrow k}(\mathbf{r})$ with equation (5) to obtain

$$\mathbf{U}^{(i)}(\mathbf{r}) = \mathbf{u}^{(i)}(\mathbf{b}^{i \rightarrow j}(\mathbf{r}), \mathbf{b}^{i \rightarrow k}(\mathbf{r})), \quad (6)$$

where $j, k \neq i$ and $j < k$.

The relaxed energy has two contributions, intralayer and interlayer energies:

$$E^{\text{tot}}(\mathbf{u}^{(1)}, \mathbf{u}^{(2)}, \mathbf{u}^{(3)}) = E^{\text{intra}}(\mathbf{u}^{(1)}, \mathbf{u}^{(2)}, \mathbf{u}^{(3)}) + E^{\text{inter}}(\mathbf{u}^{(1)}, \mathbf{u}^{(2)}, \mathbf{u}^{(3)}), \quad (7)$$

where $\mathbf{u}^{(\ell)}$ is the relaxation displacement vector in layer ℓ . To obtain the relaxation pattern, we minimize the total energy with respect to the relaxation displacement vector.

We model the intralayer coupling based on linear elasticity theory:

$$E^{\text{intra}}(\mathbf{u}^{(1)}, \mathbf{u}^{(2)}, \mathbf{u}^{(3)}) = \sum_{\ell=1}^3 \int \frac{1}{2} \left[G (\partial_x u_x^{(\ell)} + \partial_y u_y^{(\ell)})^2 + K \left((\partial_x u_x^{(\ell)} - \partial_y u_y^{(\ell)})^2 + (\partial_x u_y^{(\ell)} + \partial_y u_x^{(\ell)})^2 \right) \right] d\mathbf{b}, \quad (8)$$

where G and K are shear and bulk moduli of monolayer graphene, which we take to be $G = 47,352$ meV per unit cell, $K = 69,518$ meV per unit cell^{58,60}.

The interlayer energy accounts for the energy cost of the layer misfit, which is described by the generalized stacking fault energy (GSFE)^{61,62} obtained using first principles Density Functional Theory with the Vienna Ab initio Simulation Package^{63–65}. GSFE is the ground state energy as a function of the local stacking with respect to the lowest-energy stacking between a bilayer. For bilayer graphene, GSFE is maximized at the AA stacking and minimized at the AB stacking. Letting $\mathbf{b} = (b_x, b_y)$ be the relative stacking between two layers, we define the following vector $\mathbf{v} = (v, w) \in [0, 2\pi]^2$:

$$\begin{pmatrix} v \\ w \end{pmatrix} = \frac{2\pi}{a_0} \begin{bmatrix} \sqrt{3}/2 & -1/2 \\ \sqrt{3}/2 & 1/2 \end{bmatrix} \begin{pmatrix} b_x \\ b_y \end{pmatrix}, \quad (9)$$

where $a_0 = 2.4595$ Å is the graphene lattice constant. We parameterize the GSFE as follows:

$$\begin{aligned} V_{j\pm}^{\text{GSFE}} = & c_0 + c_1(\cos v + \cos w + \cos(v+w)) \\ & + c_2(\cos(v+2w) + \cos(v-w) + \cos(2v+w)) \\ & + c_3(\cos(2v) + \cos(2w) + \cos(2v+2w)), \end{aligned} \quad (10)$$

where we take $c_0 = 6.832$ meV per cell, $c_1 = 4.064$ meV per cell, $c_2 = -0.374$ meV per cell, $c_3 = -0.0095$ meV per cell^{58,60}. The van der Waals force is implemented through the vdW–Density Functional Theory method using the SCAN+rVV10 functional⁶⁶. In terms of $V_{\ell\pm}^{\text{GSFE}}$, the total interlayer energy can be expressed as follows:

$$\begin{aligned} E^{\text{inter}} = & \frac{1}{2} \int V_{1+}^{\text{GSFE}}(\mathbf{B}^{1 \rightarrow 2}) d\mathbf{b} + \frac{1}{2} \int [V_{2-}^{\text{GSFE}}(\mathbf{B}^{2 \rightarrow 1}) + V_{2+}^{\text{GSFE}}(\mathbf{B}^{2 \rightarrow 3})] d\mathbf{b} \\ & + \frac{1}{2} \int V_{3-}^{\text{GSFE}}(\mathbf{B}^{3 \rightarrow 2}) d\mathbf{b}, \end{aligned} \quad (11)$$

where $\mathbf{B}^{i \rightarrow j} = \mathbf{b}^{i \rightarrow j} + \mathbf{u}^{(j)} - \mathbf{u}^{(i)}$ is the relaxation modified local shift vector. Note that we neglect the interlayer coupling between layers 1 and 3. The total energy is obtained by summing over uniformly sampled configuration space. In this work, we discretize the four-dimensional configuration space by $54 \times 54 \times 54 \times 54$.

Unequal twist angles and effects of twist angle disorder

We show the relaxed supermoiré structure calculated for unequal twist angles $(\theta, 0, -\theta')$. Supplementary Fig. 7 shows the local misfit energy for $\theta = 1.8^\circ$ with varying $\theta' = 1.8^\circ, 1.75^\circ, 1.7^\circ$. The h-HTG and \bar{h} -HTG domains can be identified by the honeycomb pattern in the misfit energy. It can be seen that even a small variation in θ_{12} or θ_{23} will result in large variations in the supermoiré wavelength. However, our calculations indicate that h-HTG and \bar{h} -HTG domains still form within every supermoiré domain regardless of its size, resulting in a qualitatively equivalent structure to the equi-angle one. Therefore, we anticipate that with twist angle variations, whereas the supermoiré pattern may change substantially, physical properties attributed to h-HTG and \bar{h} -HTG moiré lattices should be robust.

We do not observe transport features at densities corresponding to the supermoiré unit cell area. This could be due to the strong dependence of the supermoiré size on the precise local twist angles. Therefore, coherent supermoiré over a few unit cells requires ultra-low twist-angle disorder, which is beyond the controllability of our current fabrication techniques.

Data availability

All the experimental data used in this work are available via Harvard Dataverse at <https://doi.org/10.7910/DVN/TVYXOI> (ref. 67). Source data are provided with this paper. All other data that support the

findings of this study are available from the corresponding authors upon reasonable request.

References

51. Wang, L. et al. One-dimensional electrical contact to a two-dimensional material. *Science* **342**, 614–617 (2013).
52. Spietz, L., Teufel, J. & Schoelkopf, R. J. A twisted pair cryogenic filter. Preprint at <https://arxiv.org/abs/cond-mat/0601316> (2006).
53. Chiba, D. et al. Electrical control of the ferromagnetic phase transition in cobalt at room temperature. *Nat. Mater.* **10**, 853–856 (2011).
54. Arrott, A. Criterion for ferromagnetism from observations of magnetic isotherms. *Phys. Rev.* **108**, 1394–1396 (1957).
55. Slater, J. C. & Koster, G. F. Simplified LCAO method for the periodic potential problem. *Phys. Rev.* **94**, 1498–1524 (1954).
56. Koshino, M. Interlayer interaction in general incommensurate atomic layers. *New J. Phys.* **17**, 015014 (2015).
57. Wilhelm, P. H., Lang, T. C., Scheurer, M. S. & Läuchli, A. M. Non-coplanar magnetism, topological density wave order and emergent symmetry at half-integer filling of moiré Chern bands. *SciPost Phys* **14**, 040 (2023).
58. Zhu, Z., Cazeaux, P., Luskin, M. & Kaxiras, E. Modeling mechanical relaxation in incommensurate trilayer van der Waals heterostructures. *Phys. Rev. B* **101**, 224107 (2020).
59. Cazeaux, P., Luskin, M. & Massatt, D. Energy minimization of two dimensional incommensurate heterostructures. *Arch. Ration. Mech. Anal.* **235**, 1289–1325 (2019).
60. Carr, S. et al. Relaxation and domain formation in incommensurate two-dimensional heterostructures. *Phys. Rev. B* **98**, 224102 (2018).
61. Kaxiras, E. & Duesbery, M. S. Free energies of generalized stacking faults in Si and implications for the brittle-ductile transition. *Phys. Rev. Lett.* **70**, 3752–3755 (1993).
62. Zhou, S., Han, J., Dai, S., Sun, J. & Srolovitz, D. J. Van der Waals bilayer energetics: generalized stacking-fault energy of graphene, boron nitride, and graphene/boron nitride bilayers. *Phys. Rev. B* **92**, 155438 (2015).
63. Kresse, G. & Hafner, J. Ab initio molecular dynamics for liquid metals. *Phys. Rev. B* **47**, 558–561 (1993).
64. Kresse, G. & Furthmüller, J. Efficiency of ab initio total energy calculations for metals and semiconductors using a plane-wave basis set. *Comput. Mater. Sci.* **6**, 15–50 (1996).
65. Kresse, G. & Furthmüller, J. Efficient iterative schemes for ab initio total-energy calculations using a plane-wave basis set. *Phys. Rev. B* **54**, 11169–11186 (1996).
66. Peng, H., Yang, Z.-H., Perdew, J. P. & Sun, J. Versatile van der Waals density functional based on a meta-generalized gradient approximation. *Phys. Rev. X* **6**, 041005 (2016).
67. Xia, L. Replication data for ‘Topological bands and correlated states in helical trilayer graphene’. *Harvard Dataverse* <https://doi.org/10.7910/DVN/TVYXOI> (2024).

Acknowledgements

We thank M. Kastner, P. Ledwith and E. Berg for helpful discussions, A. Bangura, G. Jones, R. Nowell, A. Woods and S. Hannahs for technical support and X. Wang for assistance with device fabrication. This work was partially supported by the Army Research Office MURI (grant no. W911NF2120147), the 2DMAGIC MURI (grant no. FA9550-19-1-0390), the National Science Foundation (grant no. DMR-1809802), the STC Center for Integrated Quantum Materials (NSF grant no. DMR-1231319), the Ramón Areces Foundation and the Gordon and Betty Moore Foundation’s EPIQS Initiative through grant no. GBMF9463 to

P.J.H. This work was supported by the Air Force Office of Scientific Research (AFOSR) under grant no. FA9550-22-1-0432. Measurement infrastructure was funded in part by the Gordon and Betty Moore Foundation’s EPIQS initiative through grant nos. GBMF3429 and GBMF9460. D.G.-G. gratefully acknowledges support from the Ross M. Brown Family Foundation. D.G.-G.’s involvement in measurements at Stanford and data analysis was supported by the US Department of Energy, Office of Science, Basic Energy Sciences, Materials Sciences and Engineering Division, under contract DE-AC02-76SF00515. K.W. and T.T. acknowledge support from the JSPS KAKENHI (grant nos. 21H05233 and 23H02052) and World Premier International Research Center Initiative (WPI), MEXT, Japan. A portion of this work was performed at the National High Magnetic Field Laboratory, which is supported by National Science Foundation cooperative agreement no. DMR-2128556 and the State of Florida. This work was performed in part at the Harvard University Center for Nanoscale Systems (CNS); a member of the National Nanotechnology Coordinated Infrastructure Network (NNCI), which is supported by the National Science Foundation under NSF grant no. ECCS-2025158. This work was carried out in part through the use of MIT.nano’s facilities. This work made use of the MRSEC Shared Experimental Facilities at MIT, supported by the National Science Foundation under grant no. DMR-1419807. A.U. acknowledges support from the MIT Pappalardo Fellowship and from the VATAT Outstanding Postdoctoral Fellowship in Quantum Science and Technology. Z.Z. is supported by a Stanford Science fellowship. Sandia National Laboratories is a multimission laboratory managed and operated by National Technology & Engineering Solutions of Sandia, LLC, a wholly owned subsidiary of Honeywell International Inc., for the US Department of Energy’s National Nuclear Security Administration under contract no. DE-NA000352.

Author contributions

S.C.d.l.B. and A.U. conceived the project. L.-Q.X. fabricated the devices with the help of A.U. L.-Q.X., A.U. and S.C.d.l.B. carried out the helium-3 transport measurements. A.S. and L.-Q.X. carried out the dilution refrigerator transport measurements under the supervision of D.G.-G. T.D. and Y.H.K. performed band structure, magnetization and Hartree–Fock calculations. T.D. and Z.Z. performed lattice-relaxation calculations. K.W. and T.T. supplied the boron nitride crystals. A.U., S.C.d.l.B., L.-Q.X., A.S., T.D., L.F. and P.J.-H. analysed the data and discussed the interpretation. A.U., S.C.d.l.B. and L.-Q.X. wrote the manuscript with input from all authors. P.J.-H. supervised the project.

Competing interests

The authors declare no competing interests.

Additional information

Extended data is available for this paper at

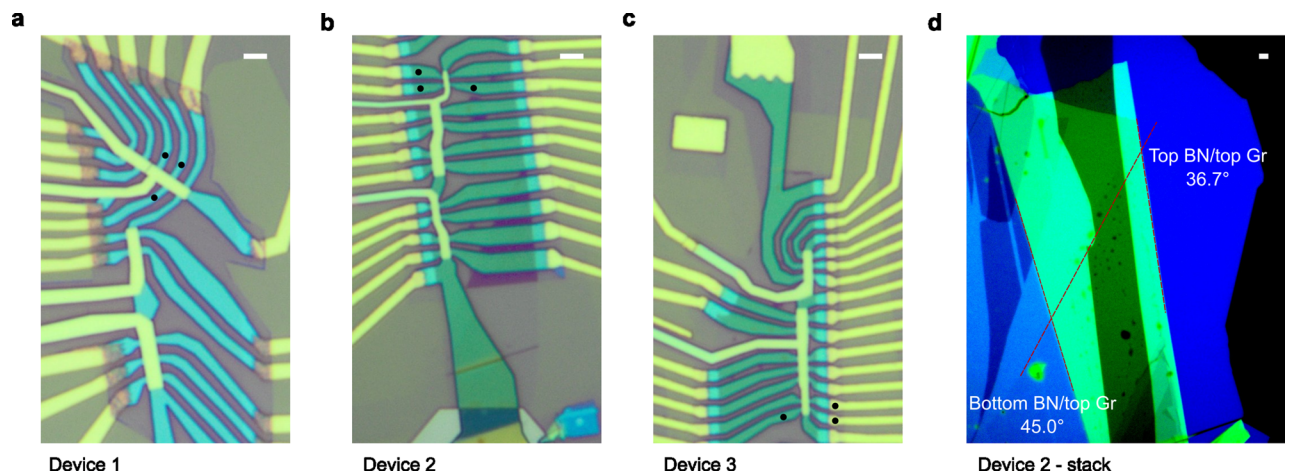
<https://doi.org/10.1038/s41567-024-02731-6>.

Supplementary information The online version contains supplementary material available at <https://doi.org/10.1038/s41567-024-02731-6>.

Correspondence and requests for materials should be addressed to Li-Qiao Xia, Sergio C. de la Barrera, Aviram Uri or Pablo Jarillo-Herrero.

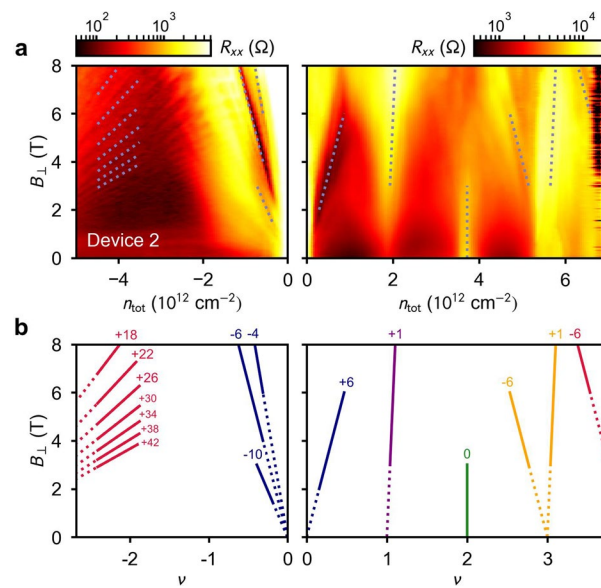
Peer review information *Nature Physics* thanks Ipsita Das and the other, anonymous, reviewer(s) for their contribution to the peer review of this work.

Reprints and permissions information is available at www.nature.com/reprints.



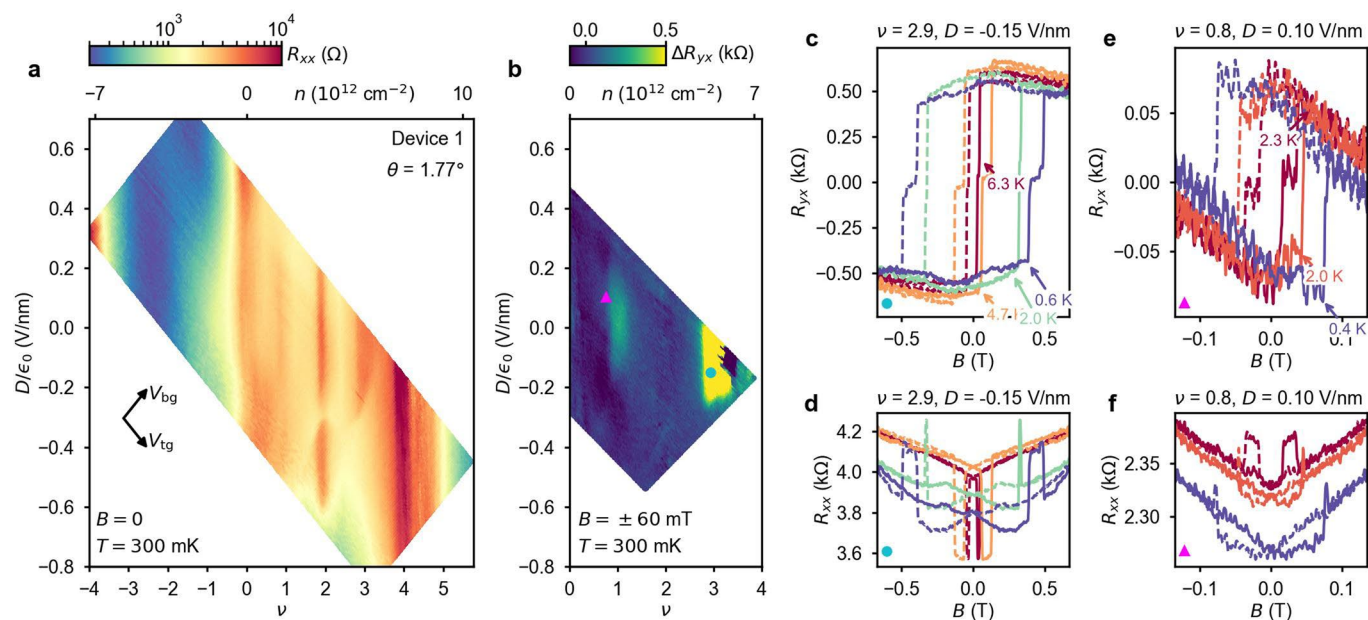
Extended Data Fig. 1 | Optical micrographs of HTG devices. **a**, Device 1 - a secondary device with $\theta = 1.77^\circ$. **b**, Device 2 - our main device with $\theta = 1.79^\circ$. **c**, Device 3. This device shares the van der Waals heterostructure with Device 2. R_{xx} and R_{yx} contacts are indicated by black dots for all devices. **d**, Contrast-enhanced

Device 3
optical micrograph of Device 2 after stacking. The crystallographic edges of the top hBN, bottom hBN, and top monolayer graphene are highlighted, showing no accidental alignment between hBN and HTG. All scale bars are $2\mu\text{m}$.



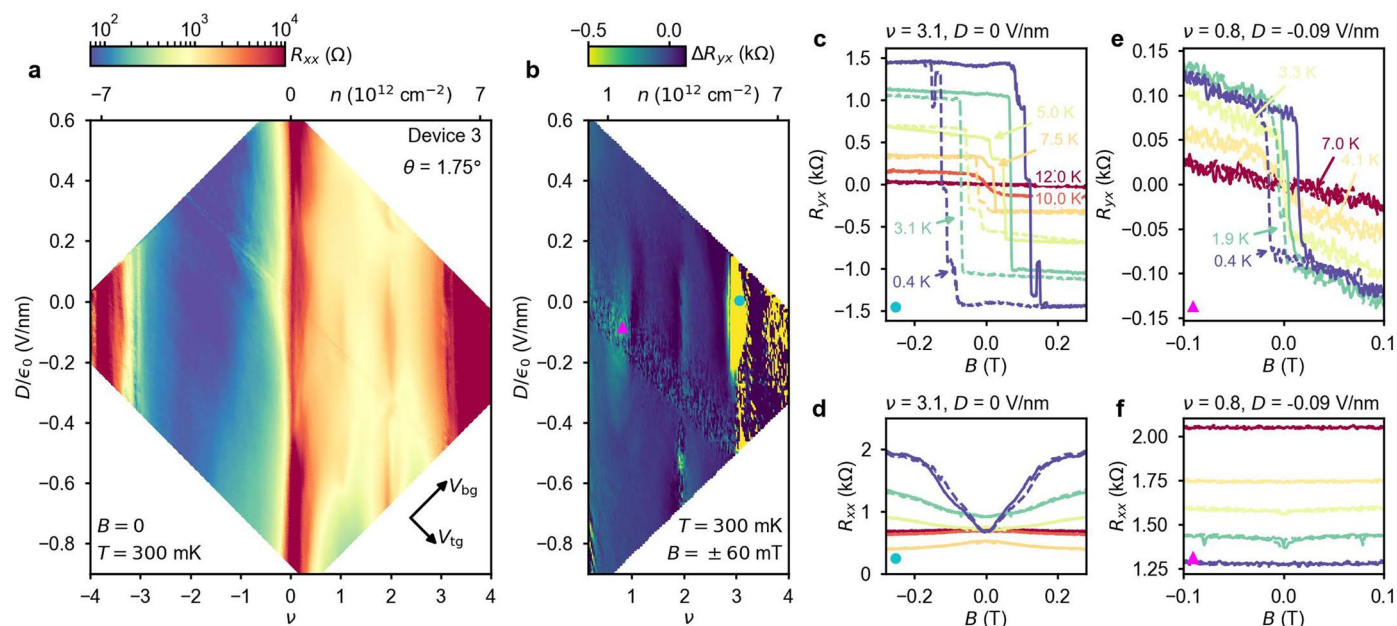
Extended Data Fig. 2 | Twist angle determination. a, R_{xx} Landau fan from Device 2, measured at $D = 0$ and $T = 300$ mK. Electron-side (right) and hole-side (left) are plotted with different color scales to improve contrast. Dashed lines correspond

to the best-fit series shown in **b**. **b,** Map of the best-fit slopes from a emerging from a consistent set of integer fillings, ν . Red lines emerge from $n_{\nu=\pm 4}$ and $\nu = \pm 4$ (off-scale due to measurement limitations) in **a** and **b**, respectively.



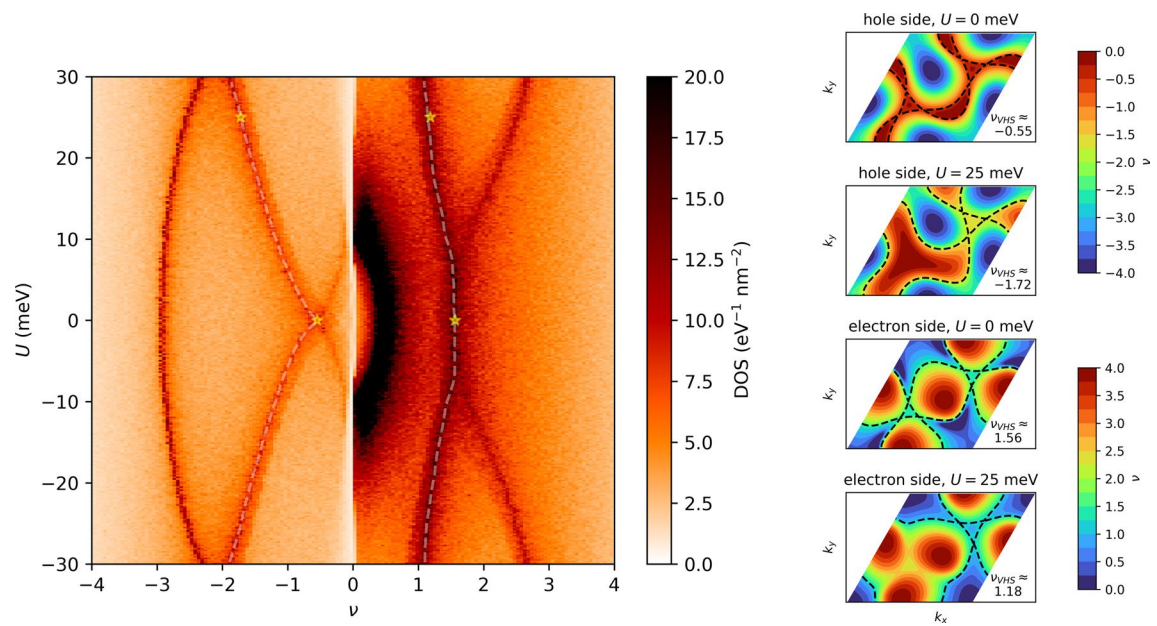
Extended Data Fig. 3 | Device 1 characterization. **a**, R_{xx} versus n and D , showing resistance peaks at charge neutrality ($\nu = 0$), at the moiré band gaps ($\nu = \pm 4$), and at the correlated states at $\nu = 1, 2, 3$. **b**, Field-trained ΔR_{yx} measured at $T = 300 \text{ mK}$ and $B = \pm 60 \text{ mT}$ versus ν and D . Hot spots near $\nu = 1, 3$ indicate AHE.

c, d, Field-antisymmetrized R_{yx} and field-symmetrized R_{xx} taken at $\nu = 2.9$ (cyan circle in **b**) and $D/\epsilon_0 = -0.15 \text{ V/nm}$ while sweeping B up (solid) and down (dashed) at different temperatures as indicated. Temperature colorcode in **d** is identical to **c**. **e, f**, Same as **c, d**, taken at $\nu = 0.8$ and $D/\epsilon_0 = 0.1 \text{ V/nm}$ (pink triangle in **b**).



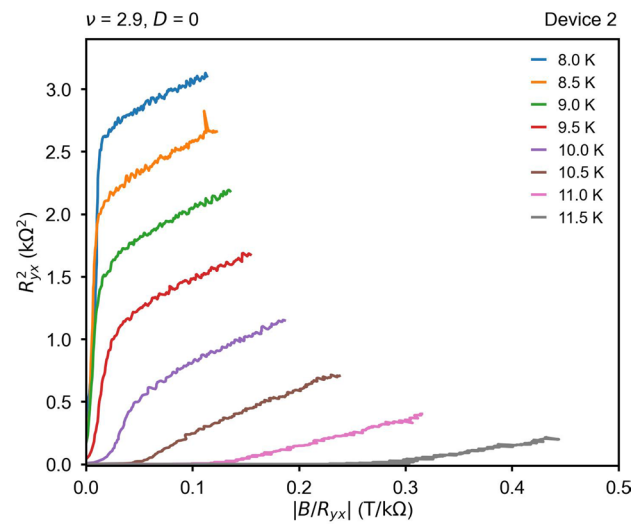
Extended Data Fig. 4 | Device 3 characterization. **a**, R_{xx} versus n and D , showing resistance peaks at charge neutrality ($\nu=0$), at the moiré band gaps ($\nu=\pm 4$), and at the correlated states at $\nu=1,2,3$. The contact resistance becomes very large when $\nu \geq 3.2$, leading to artifacts in the data. **b**, Field-trained ΔR_{yx} measured at $T = 300 \text{ mK}$ and $B = \pm 60 \text{ mT}$ versus ν and D . Hot spots near $\nu=1,3$ indicate AHE.

c,d, Field-antisymmetrized R_{yx} and field-symmetrized R_{xx} taken at $\nu=3.1$ (cyan circle in **b**) and $D/\epsilon_0 = 0$ while sweeping B up (solid) and down (dashed) at different temperatures as indicated. The temperature color code in **d** is identical to **c**. **e,f**, Same as **c,d**, taken at $\nu=0.8$ and $D/\epsilon_0 = -0.09 \text{ V/nm}$ (pink triangle in **b**).

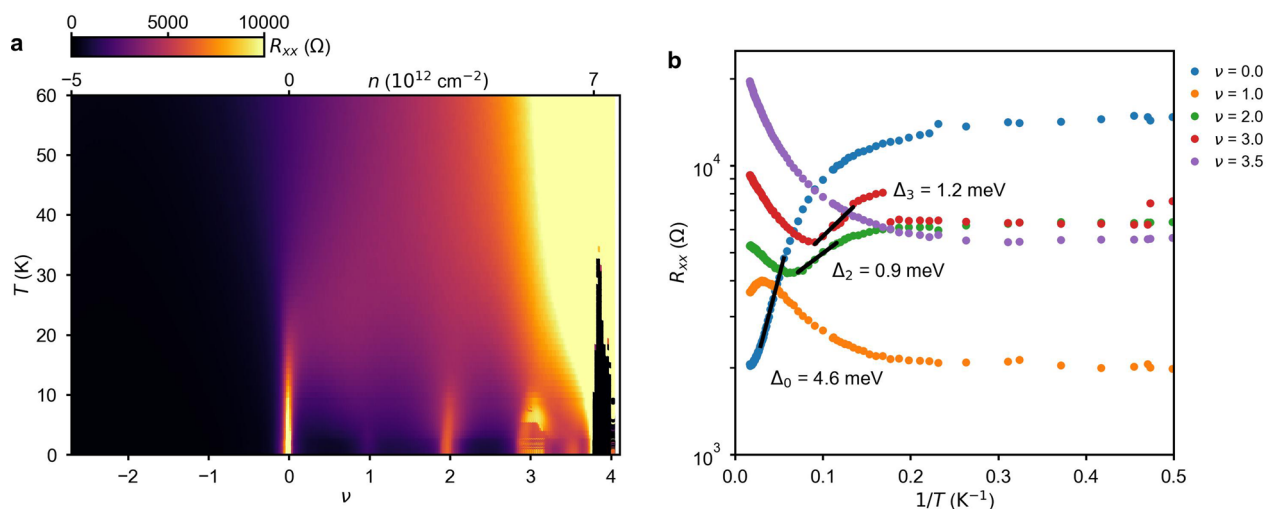


Extended Data Fig. 5 | Single-particle density of states and Van Hove singularity. (left) The single particle DOS with momentum-dependent tunneling as a function of filling factor and layer potential. The Van Hove singularity at

which the Hall density switches sign is indicated by the dashed lines. (right) Extended Fermi surfaces at the Van Hove singularity are shown for the four points indicated by stars in the DOS plot.



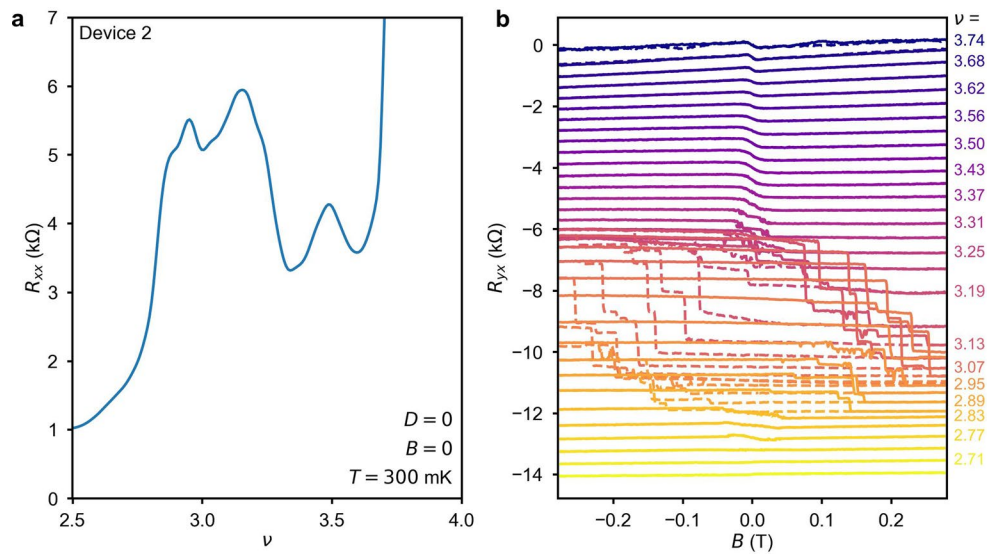
Extended Data Fig. 6 | Extraction of the Curie temperature using an Arrott plot. R_{yx}^2 versus $|B/R_{yx}|$. Positive (negative) extrapolated intercept of the linear part at high B indicates a ferromagnetic (paramagnetic) state. The curve taken at $T = 10.5$ K has approximately zero intercept, indicating a Curie temperature $T_C \approx 10.5$ K.



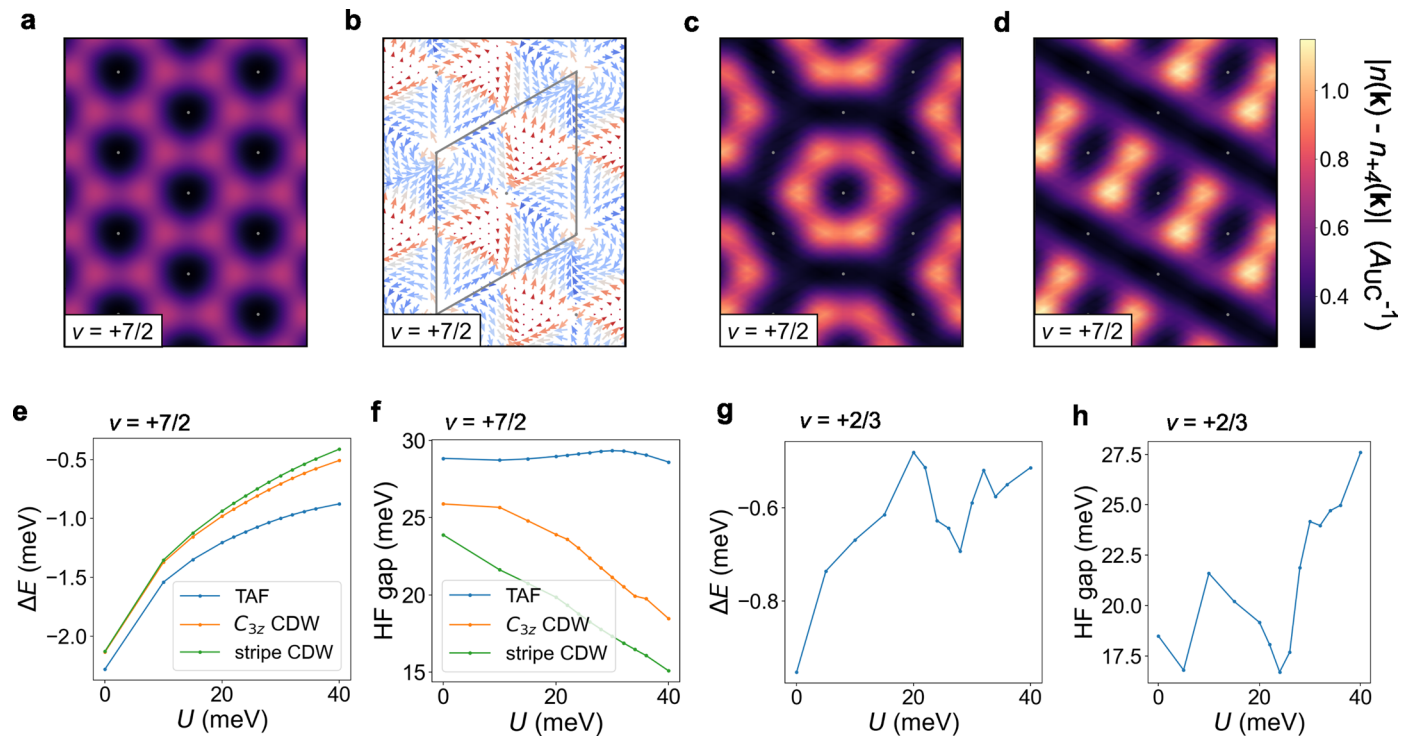
Extended Data Fig. 7 | Temperature dependence and gap sizes estimation.

a, R_{xx} (raw data, not field-symmetrized) versus ν and T of Device 2 at $D=0$ and $B=0$. The jumps in resistance near $\nu=3$ reflect the AHE of different magnetic states combined with R_{yx} mixing. A pronounced electron-hole asymmetry is demonstrated. **b**, line cuts of **a** versus $1/T$ at different ν as indicated. Some curves show non-monotonic temperature dependence due to the parallel conduction of the insulating domains and the metallic network of domain walls. The total resistance can be modelled by $R_{\text{tot}} = (R_M^{-1} + R_I^{-1})^{-1}$, where R_M and R_I are the resistance of the metallic walls and insulating domains, respectively. When one of the resistances is much smaller than the other, we have $R_{\text{tot}} \approx \min(R_M, R_I)$. At low

temperatures, $1/T \gtrsim 0.2 \text{ K}^{-1}$, the insulating bulk is shunted by the metal, saturating the increased resistance of the insulating domains. As T is increased to intermediate values, $1/T \sim 0.1 \text{ K}^{-1}$, the domains become less resistive and $R_{\text{tot}} \approx R_I$. We use this regime to estimate the gap sizes for $\nu=0, 2, 3$ (indicated) by fitting the data to $R = R_0 \exp\{-\Delta_\nu/2k_B T\}$, where Δ_ν is the gap at filling ν and k_B is Boltzmann's constant. At higher temperatures, $1/T \lesssim 0.05 \text{ K}^{-1}$ for $\nu=2, 3$, the correlated states give way to a metallic phase, accounting for the increasing resistance with T at those filling factors. At $\nu=1$, evidence for thermal activation is absent, indicating a semimetallic state without a fully developed correlated gap.



Extended Data Fig. 8 | Correlated state at $\nu=7/2$. **a**, R_{xx} versus ν , measured on Device 2 at $D=0$, $B=0$, and $T=300$ mK. At $\nu=7/2$, we find a resistance peak distinct from the one at $\nu=3$. **b**, Waterfall plot of antisymmetrized R_{yx} taken by sweeping B up (solid) and down (dashed) as the fast axis at $D=0$ and different ν , as indicated on the right of every other curve. The AHE persists beyond $\nu=7/2$.



Extended Data Fig. 9 | Hartree-Fock calculations at $\nu=7/2$ and $2/3$. **a**, Charge density $n(\mathbf{r})$ (measured relative to that at full flat band filling $n_{\nu=+4}(\mathbf{r})$) of the tetrahedral antiferromagnet (TAF) at $\nu=7/2$. Grey dots indicate ABA-stacking regions. **b**, Local spin orientation in the TAF. Arrows denote spin direction in s_x-s_y plane, while red (blue) coloring indicates out-of-plane polarization along $+\hat{s}_z$ ($-\hat{s}_z$). Grey parallelogram indicates the new quadrupled moiré unit cell. **c,d** Same as **a** except for the \hat{C}_{3z} charge density wave and stripe charge density

wave respectively. **e**, ΔE of the different translation symmetry breaking solutions at $\nu=7/2$ as a function of interlayer potential U . ΔE is measured relative to that of the best translation-symmetric solution. **f**, Charge gap of the translation symmetry breaking solutions at $\nu=7/2$. **g,h**, Same as **e,f** except for the best translation symmetry breaking solution at $\nu=2/3$. All calculations performed on a 18×18 system using $\theta = 1.80^\circ$, $w_{AA} = 75$ meV.